02,10

Superconductivity of nanostructured Ga-Sn alloy

© M.V. Likholetova[1], E.V. Charnaya[1,¶], M.A. Annageldiev[1], V.M. Mikushev[1], Yu.A. Kumzerov[2], A.V. Fokin[2]

[1] St. Petersburg State University,
St. Petersburg, Russia
[2] Ioffe Institute,
St. Petersburg, Russia

¶ E-mail: e.charnaya@spbu.ru

Received May 14, 2024
Revised May 14, 2024
Accepted May 15, 2024

The paper presents studies of superconductivity of the eutectic gallium-tin alloy embedded into pores of the opal matrix. Low-temperature measurements of the dc and ac magnetizations were carried out within a wide range of magnetic fields. Three superconducting transitions were observed. The constructed $H-T$ phase diagram demonstrated the positive curvature of the critical lines at small magnetic fields. It was explained using a model, which takes into account the proximity effect. For two transitions, it was shown that the motion of superconducting vortices was thermally activated. Arrhenius plots were constructed and activation energies for different bias fields were calculated. The sharp decrease in the activation barriers was observed at the same range of magnetic fields as the change in the critical lines curvature, which was ascribed to transformations in the superconducting vortex system.

Keywords:: binary Ga-Sn alloy, superconductivity, nanocomposite, magnetic properties.

DOI: 10.61011/PSS.2024.06.58706.124

1. Introduction

Currently the studies of gallium-containing alloys are actively carried out. They are promising materials in pharmaceuticals, medicine, nanoelectronics and other fields due to their properties such as low melting point, stable electrical properties, high thermal conductivity and non-toxicity [1,2]. Gallium-containing alloys are broadly used as low-temperature solders and are also considered for the creation of various superconducting nano-electronic elements [3,4], such as self-healing superconducting contacts and wires. The alloys Ga-In-Sn, Ga-In and Ga-Sn are of particular interest due to the prospects of application as a superconducting solder. However, to date, the superconductivity of the Ga-Sn alloy has been poorly studied, in contrast to the more thoroughly studied Ga-In-Sn and Ga-In alloys. The superconductivity of only bulk Ga-Sn with different ratios of gallium and Sn [5] and an alloy close in composition to the eutectic point introduced into a silica opal matrix [6] has been studied.

Nanostructuring and, in particular, nanoconfinement conditions significantly influence the superconductivity of metals and metallic alloys, which is manifested in changes in the values of critical temperatures, critical magnetic fields, critical currents, etc. [7–9]. Various theories have been proposed to explain this behavior [10]. A change of superconductivity was also revealed in eutectic nanostructured gallium-containing alloys compared to bulk alloys [6,11,12]. Two diffused superconducting transitions were found in the nanostructured Ga-Sn in an opal matrix with the size of silicate spheres approximately 150 nm at temperatures 6.4 and 4.7 K [6], whereas for a bulk eutectic alloy, there was one sharp transition to a superconducting state at temperature, close to the critical temperature of bulk Sn (3.72 K) [5]. The Ga-Sn alloy embedded into an opal matrix with a diameter of silicate balls $\sim$ 500 nm was studied in this paper with the aim of studying the impact of morphology on the superconductivity of the eutectic alloy Ga-Sn in more detail. Static (DC) and dynamic (AC) magnetizations were measured in a wide range of magnetic fields in the temperature range of the alloy superconductivity.

2. Experiment

The nanocomposite is an alloy of gallium and Sn of eutectic composition (91.5 at.% Ga, 8.5 at.% Sn) [13], embedded in the pores of an opal matrix. The average diameter of silicate spheres, equal to 500 nm, was determined from an image of an empty opal matrix obtained on a Zeiss Merlin scanning electron microscope (Figure 1). The matrix is a cubic close packing of amorphous silica spheres with octahedral and tetrahedral pores. The sizes of octahedral and tetrahedral pores calculated for the case of an ideal opal matrix are 113 and 207 nm. Pores occupy 26% of the total matrix volume.

The liquid eutectic alloy Ga-Sn was introduced into the voids of the matrix under high pressure up to 10 kbar. The filling factor was evaluated from the difference in mass of the empty and filled matrix and was approximately 85%. Plates weighing 248.51 and 54.84 mg were cut from the obtained nanocomposite to measure DC and AC magnetization, respectively.

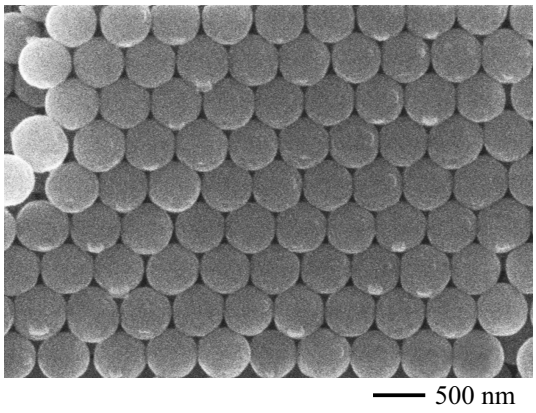

Figure 1. Scanning electron microscopy image of an empty opal matrix.

Measurements of the temperature dependences of the specific DC magnetization M_{DC} were carried out on a vibration SQUID magnetometer MPMS 3 (Quantum Design Inc.) in the temperature range from 1.8 to 10 K and in magnetic bias fields H_{DC} from 10 to 10 kOe. The temperature dependences of magnetization were obtained in the heating mode in a magnetic field being preliminary zero-field cooled (ZFC), subsequent mode of field-cooled cooling (FCC) and in the mode of field-cooled warming (FCW). The isothermal field dependences of static magnetization M_{DC} were also measured in magnetic fields from −70 to 70 kOe at temperatures 1.8, 5 and 7 K. The temperature dependences of the real M'_{AC} and imaginary M''_{AC} parts of the specific AC magnetization were obtained using measuring system PPMS-9+Evercool II (Quantum Design Inc.) in the temperature range from 1.9 to 10 K in the FCC mode in magnetic bias fields from 0 to 5 kOe and with the application of an alternating magnetic field of amplitude $H_{AC} = 1$ Oe and frequency f from 90 Hz to 7 kHz. At zero bias field, the temperature dependences of the AC magnetization were also measured at various H_{AC} in the range from 0.1 to 10 Oe. DC susceptibility was calculated as $\chi_{DC} = M_{DC}/H_{DC}$. The real and imaginary parts of the AC susceptibility were calculated as $\chi'_{AC} = M'_{AC}/H_{AC}$ and $\chi''_{AC} = M''_{AC}/H_{AC}$, respectively.

X-ray spectra were obtained using an Ultima IV diffractometer (Rigaku) with CuK_α radiation at temperatures from 305 to 150 K. For X-ray diffraction analysis, the PDXL (Rigaku) and Topas 5.0 (Bruker GmbH) software packages and the ICDD PDF-2 2020 and ICSD 2021 databases were applied.

3. Results

The dependences of ZFC susceptibility on temperature for various magnetic bias fields are presented in Figure 2. There are three superconducting transitions with the corresponding critical temperatures T_{c1}, T_{c2} and T_{c3} in the curves. The transitions are diffused, and the degrees of magnetic field shielding after the transitions differ significantly. Almost the entire volume of the nanocomposite is shielded from the external magnetic field in a field of 10 Oe at a temperature of 1.8 K. After the first and second transitions, only a small fraction of the sample volume is shielded. The critical temperatures decrease and the transitions become

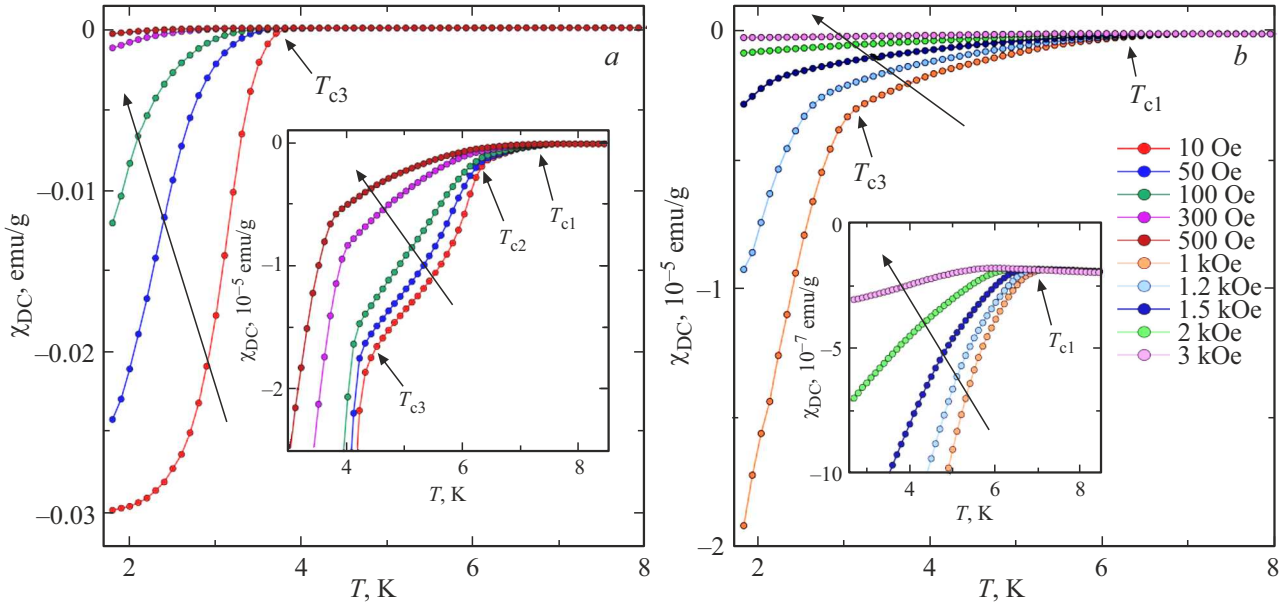

Figure 2. The temperature dependences of the DC susceptibility of χ_{DC} in magnetic fields: *a* — from 10 to 500 Oe and *b* — from 1 to 3 kOe, obtained in the ZFC mode. The inset *a* shows the region of three superconducting transitions on an enlarged scale for fields from 10 to 500 Oe. The inset *b* shows the region of the high-temperature transition on an enlarged scale for field from 1 to 3 kOe. The arrows indicate an increase of field.

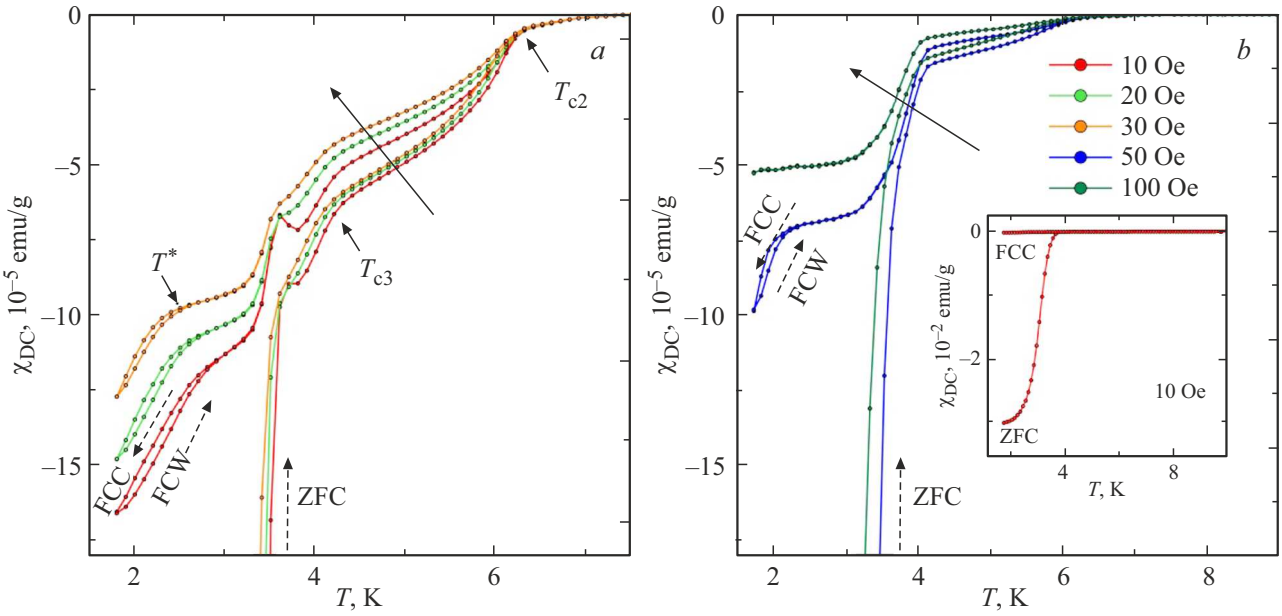

Figure 3. The temperature dependences of DC susceptibility χ_{DC}, obtained in ZFC, FCC and FCW modes when applying bias fields: *a* — from 10 to 30 Oe and *b* — 50 and 100 Oe. Dashed arrows indicate the direction of the curves, solid arrows indicate an increase of the magnetic field. The inset shows the ZFC and FCC curves in a field of 10 Oe on a reduced scale.

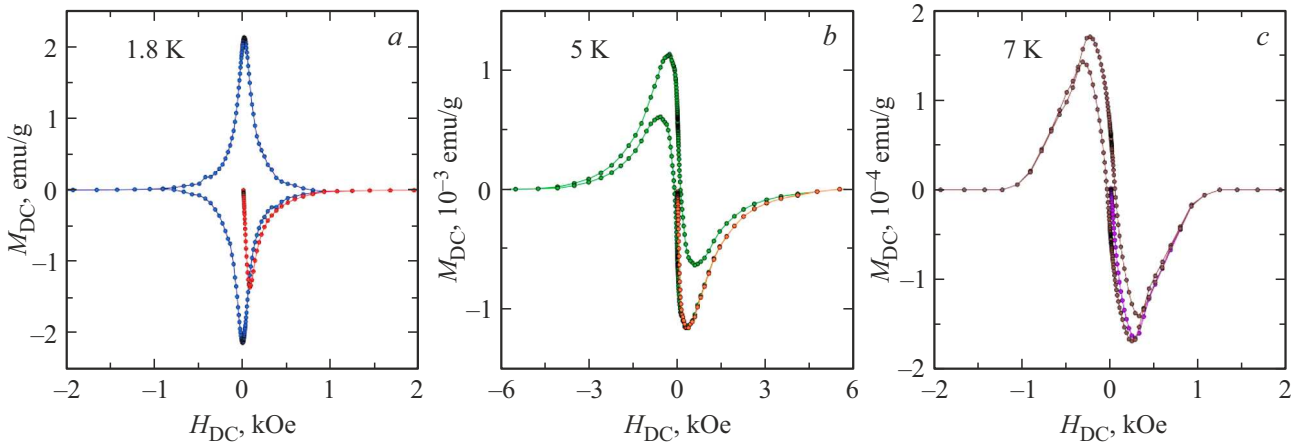

Figure 4. Isothermal field dependences of the specific DC magnetization of M_{DC} at temperatures 1.8 (*a*), 5 (*b*) and 7 K (*c*). The primary magnetization curves are shown in red, orange and purple in the online figures.

more diffused with an increase of the magnetic field. The first and second transitions merge in the fields over 100 Oe. A clear low-temperature transition is observed at temperature T_{c3} for magnetic fields up to 1.5 kOe inclusive. The critical temperature T_{c3} shifts below 1.8 K at higher magnetic fields. The following critical temperatures were determined based on the temperatures at which the ZFC curve begins to deviate for the field 10 Oe: $T_{c1} = 7.7 \pm 0.1$, $T_{c2} = 6.3 \pm 0.1$ and $T_{c3} = 4.3 \pm 0.1$ K.

Figure 3 shows that the ZFC and FCC curves diverge below the second transition. However, the curves are still close to each other at temperatures between T_{c2} and T_{c3}. A more significant divergence of the curves can be seen below T_{c3}. The difference between the values of the ZFC and FCC susceptibilities is significant at a temperature of 1.8 K (176 times for a field of 10 Oe), which indicates a strong pinning of superconducting vortices. Steps on the FCC and FCW curves are observed at a temperature designated as T^* below T_{c3} in fields up to 50 Oe inclusive. There is the hysteresis between these curves at the temperatures below T^*. The values of FCW susceptibility are less than those of FCC susceptibility in the hysteresis region. The FCC and FCW curves merge with each other, and there is no hysteresis in magnetic fields above 100 Oe. A reproducible peak is observed on the FCC and FCW curves near the third superconducting transition in the fields of 10 and 20 Oe, which blurs out with an increase of the magnetic field.

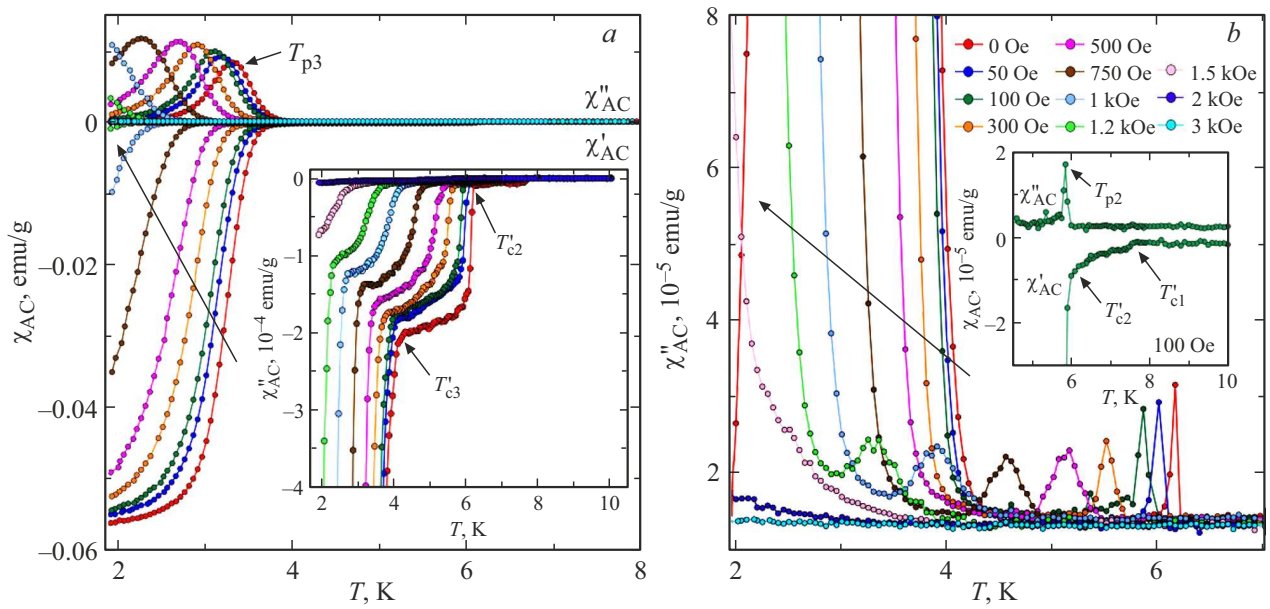

Figure 5. Temperature dependences: *a* — real (χ'_{AC}) and imaginary (χ''_{AC}) parts of the AC susceptibility, *b* — increased scale of the $\chi''_{AC}(T)$ dependence in the T_{p2} peak region for different bias magnetic fields. Inset (*a*) shows the $\chi'_{AC}(T)$ dependence on an enlarged scale in the region of critical temperatures T'_{c2} and T'_{c3}. Inset (*b*) presents the temperature dependence of χ'_{AC} and χ''_{AC} for a field of 100 Oe in the region of the T_{p2} peak and the critical temperatures T'_{c1} and T'_{c2}. Alternating field amplitude $H_{AC} = 1$ Oe, alternating field frequency was 1 kHz. The arrows indicate an increase of field.

Figure 4 shows the isothermal field dependences of the specific DC magnetization $M_{DC}(H)$ at three temperatures. A partially reversible behavior is observed at the $M_{DC}(H)$ hysteresis at 5 and 7 K, indicating the presence of weak pinning of superconducting vortices in the nanocomposite. The hysteresis is irreversible at 1.8 K, which indicates strong pinning of vortices in accordance with the results obtained from the temperature dependences of the DC susceptibility.

The temperature dependence of the real part of the AC susceptibility also shows three transitions to the superconducting state at temperatures T'_{c1}, T'_{c2} and T'_{c3} (Figure 5). The transitions are sharper, in contrast to the results obtained with the SQUID magnetometer, due to the lower sensitivity of PPMS-9. There is the transition at the temperature T'_{c2} in magnetic fields up to 1.5 kOe, in contrast to the data obtained for DC susceptibility. T'_{c1}, T'_{c2} and T'_{c3} were defined as temperatures at which there was a sharp deviation in the temperature dependence of AC susceptibility. The critical temperatures were equal to $T'_{c1} = 7.7$, $T'_{c2} = 6.2$ and $T'_{c3} = 4.3$ K in a zero bias field. It should be noted that there is no step at temperature T^* in the temperature dependences of the real part of the AC susceptibility.

There are two peaks on the imaginary part of the AC susceptibility: a very weak peak related to the second phase transition at T_{p2}, and an intense peak at T_{p3} related to the third, low-temperature phase transition. There is no peak related to the first phase transition, apparently because of the small amplitude. The peak positions shift to the region of lower temperatures with an increase of the bias magnetic field. It should be noted that the peak moves faster at T_{p2} than at T_{p3}, resulting in the two peaks being superimposed in high magnetic fields.

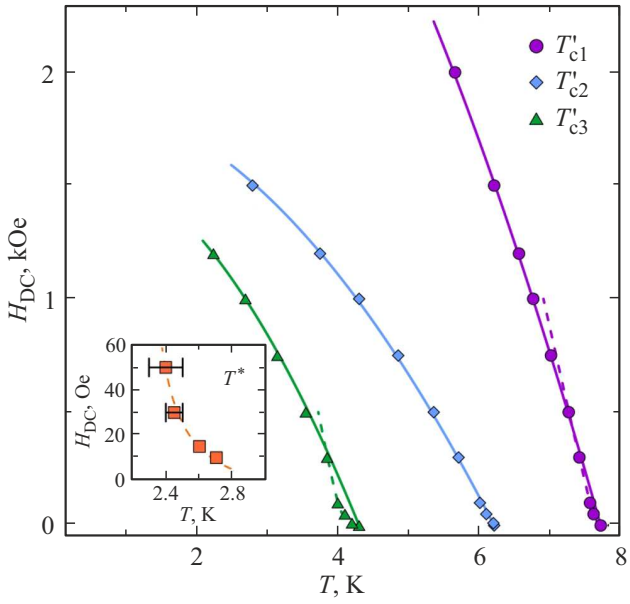

Figure 6. Phase diagram of $H-T$. Solid lines show the fitting curves constructed using the two-fluid model, and dashed lines show the curves constructed using the model taking into account the proximity effect. The inset shows T^* as a function of field.

For convenience, the critical temperatures for constructing a phase diagram in the field-temperature plane were found from the AC data, since the superconducting transi-

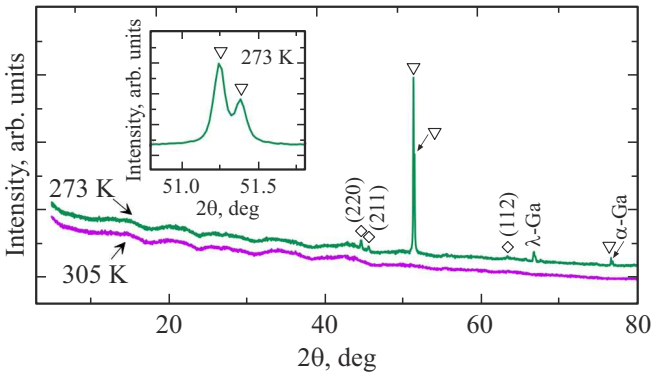

Figure 7. X-ray spectra obtained at temperatures of 305 and 273 K. Diamonds indicate peaks related to Sn, triangles indicate previously unobserved modifications of gallium. The inset shows part of the X-ray diffraction pattern at a temperature of 273 K.

tions observed in the temperature dependences of the AC susceptibility are not as smeared as for the DC susceptibility (Figure 6).

X-ray diffraction patterns were obtained at several temperatures in the cooling mode from 305 to 150 K. Figure 7 shows the spectra at two temperatures. The alloy of Ga-Sn in the opal pores is in a molten state at 305 K. Several peaks appear corresponding to the crystallized alloy after cooling to 273 K. There are no additional peaks in case of further cooling to 150 K.

4. Discussion

One transition to the superconducting state was observed when studying a bulk alloy of gallium and Sn of various compositions [13]. It was shown that with an increase of Sn concentration to 10 at.%, the transition temperature increased, and at higher concentrations, the superconductivity temperature was in the range from 3.7 to 4.2 K. Such temperatures are attributable to the formation of Sn-enriched segregates during the alloy crystallization. Three superconducting transitions over 4 K have been identified in this work. The temperature T_{c3} is close to the superconductivity temperature of bulk Sn (3.72 K) and to the transition temperature which was in the bulk alloy. The temperatures T_{c2} and $T_{c1}$are significantly higher than the superconducting transition temperature in α-Ga, equal to 1.08 K.

Other crystalline structures of gallium with significantly higher temperatures for emerging superconductivity [14–18] can appear in addition to the stable α-Ga, under the impact of various factors (high pressure, reduction in size, etc.). The X-ray diffraction patterns obtained below 273 K (Figure 7) contain two narrow peaks at $2\theta = 44.54$ and 45.52° and a weak peak at $2\theta = 63.14^\circ$, which belong to the tetragonal Sn phase with space symmetry group $I4_1/amd$. The peak at $2\theta = 76.63^\circ$ is related to α-Ga. The peak at $2\theta = 66.61^\circ$ can be related to the tetragonal structure of gallium, designated in the work [14] as λ-Ga. This structure was previously observed for Ga-Sn in another opal matrix [6]. Other peaks related to α- and λ-Ga are not visible in the X-ray diffraction patterns of the nanocomposite, most likely due to the strong disorder of the crystal structure. The peaks at $2\theta = 51.26$, 51.46 and 76.42° were not observed previously. Their occurrence may be associated with the formation of an unknown gallium structure in opal pores, induced by nano-confinement.

In accordance with the obtained X-ray diffraction patterns and the results from [6], it can be assumed that the second phase transition with a temperature of 6.3 K in low fields refers to the transition to the superconducting state of gallium-rich segregates with the structure λ-Ga, the critical temperature for which lies in the range from 6.2 to 6.5 K [7]. The total number of such segregates is relatively small in accordance with the weak shielding of the magnetic field, as in the work [6], and the low intensity of the corresponding X-ray peak. The superconducting transition at $T_{c3} = 4.3$ K is due to the presence of Sn-enriched segregates. The increase of transition temperature compared to bulk Sn can be attributed to size effects.

The appearance of superconductivity at approximately 7.7 K previously was observed in case of a nanostructured gallium [9,19–21]. The very weak diamagnetism resulting from the transition at T_{c1} indicates a very small amount of structural modification of gallium responsible for this transition. Thus, it should be assumed that the modification of gallium, which corresponds to intense peaks marked by triangles in the X-ray diffraction pattern (Figure 7), cannot be associated with the first superconducting transition.

The significant divergence between the ZFC and FCC curves below the third superconducting transition and the irreversible nature of the $M_{DC}(H)$ hysteresis indicate the presence of strong pinning of superconducting vortices in a dirty type-II superconductor. There is a weak vortex pinning in the temperature region between the first and third superconducting transitions, since there is a weak divergence between the ZFC and FCC curves and a partially reversible behavior of the $M_{DC}(H)$ hysteresis loop.

The divergences between the FCC and FCW curves obtained during cooling and heating were observed experimentally very rarely. Similar hysteresis loops were predicted in [22] and were experimentally detected for some type-II superconductors [6,12,23]. Another type of hysteresis behavior between the FCC and FCW magnetizations was demonstrated in [24], where the FCC curve ran below the FCW curve. The peaks that appear in the FCC and FCW curves at low magnetic fields near the third phase transition occur also rarely and can be explained by the paramagnetic Meissner effect (PME) [12,25,26].

The $H-T$ phase diagram (Figure 6) shows a positive curvature of the critical lines $T'_{c1}(H)$ and $T'_{c3}(H)$ in magnetic fields up to 300 Oe. The curvature changes and becomes negative as the magnetic field increases. The negative curvature of the lines of the upper critical field H^n_{c2} (n is the ordinal number of the transition) on the phase diagram

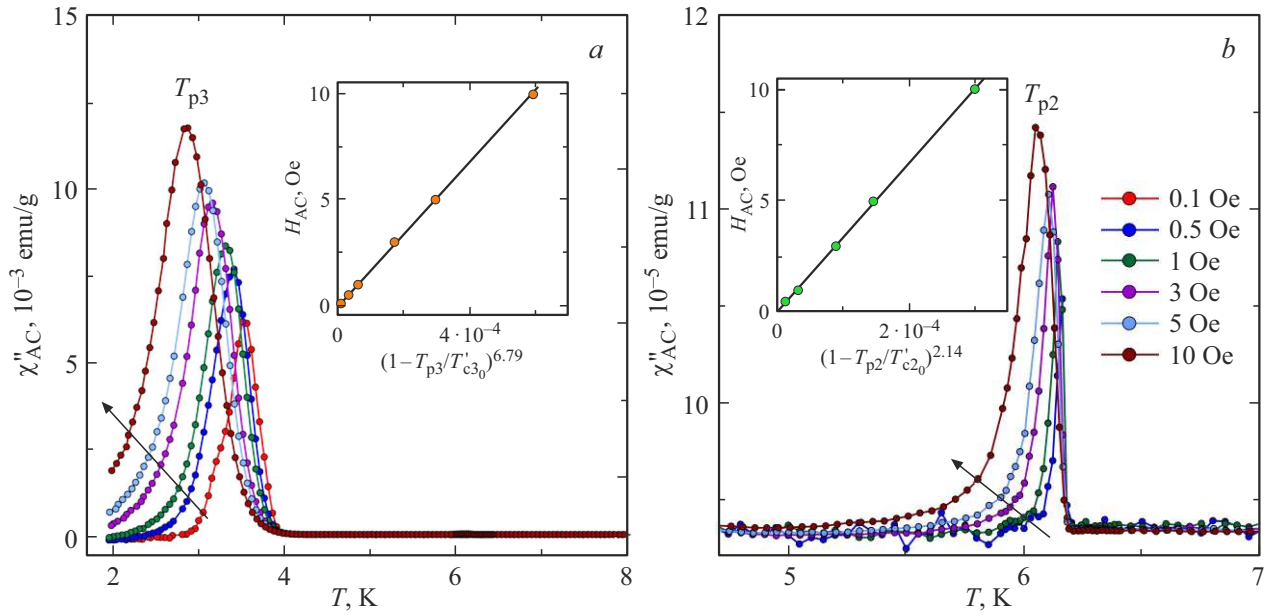

Figure 8. The temperature dependence of the imaginary part of the AC susceptibility χ''_{AC} in the zero bias field in the region of the third transition (a) and the second transition (b). The arrows indicate the direction of increase of the amplitude of the alternating field H_{AC}. The insets show the dependence of the peak positions on H_{AC}.

is described within the framework of the two-fluid model by the following expression:

$$H^n_{c2}(T) = H^n_{c2}(0)\left(1 - \left(\frac{T}{T'_{cn_0}}\right)^2\right), \qquad (1)$$

where $H^n_{c2}(0)$ is the upper critical field at zero temperature, T'_{cn_0} is the temperature of the n-th transition in the zero field.

The critical dependences for the first and third transitions for high DC fields and for the second transition in the entire range of fields are well described by expression (1), which allowed to determine the values of the upper critical fields $H^1_{c2}(0) = 4.3$, $H^2_{c2}(0) = 1.9$ and $H^3_{c2}(0) = 1.65$ kOe. Therefore, the values of the coherence length ξ_n can be estimated according to the Ginzburg-Landau theory:

$$\xi_n(0) = \sqrt{\frac{\Phi_0}{2\pi H^n_{c2}(0)}}, \qquad (2)$$

where Φ_0 is the flux quantum.

The following values were obtained for coherence lengths: $\xi_1(0) = 28$, $\xi_2(0) = 42$ and $\xi_3(0) = 45$ nm. The calculated coherence lengths are lower than the opal pore size, which is likely due to the size of the segregates.

There was positive curvature of critical lines in many bulk and nanostructured type II superconductors [6,7,11,12,14,18,24]. The paper [27] described a model taking into account the impact of the proximity effect which allows describing the positive curvature of critical lines. The fitting curve obtained by formula (13) from [27] is shown by a dashed line in Figure 6.

Figure 8 shows the temperature dependences of the imaginary part of the AC susceptibility obtained by applying an alternating field of varying amplitude H_{AC} and frequency 1 kHz in a zero constant field. It can be seen that with an increase of H_{AC} both peaks shift to lower temperatures. The dependence of the position of the peaks T_{p2} and T_{p3} on the amplitude of the AC field is described by power-law dependences: for the second phase transition $H_{AC} \propto (1 - T_{p2}/T'_{c2_0})^{2.14}$, and for the third phase transition $H_{AC} \propto (1 - T_{p3}/T'_{c3_0})^{6.79}$, where T'_{c2_0} and T'_{c3_0} are the second and third critical temperatures in the zero DC field. A power function of the peak positions on the AC amplitude is predicted for nanostructured superconductors, treated as a set of superconducting granules [28,29]. The figure shows that the exponents are higher than those in [29], but are consistent with the results [12,24].

The weak dependence of the AC susceptibility on the frequency of the alternating field and the significant influence of the amplitude of the AC field indicate the thermally activated motion of superconducting vortices. The temperatures T_{p2} and T_{p3} were determined on the imaginary part of the AC susceptibility for different frequencies of the AC field and Arrhenius curves were constructed (insets to Figure 9). Activation energies were calculated for various bias fields (Figure 9) from the slope of these curves. It was not possible to calculate activation energies for all fields because the peak at T_{p2} is weak.

The field dependence of the activation energy shows a change in the caracter of the dependence for both transitions. The dependence of magnitude of activation barriers on the field is described by the expression $U_a \propto H^{-\alpha}$. There is a weak dependence of the activation energy on the field

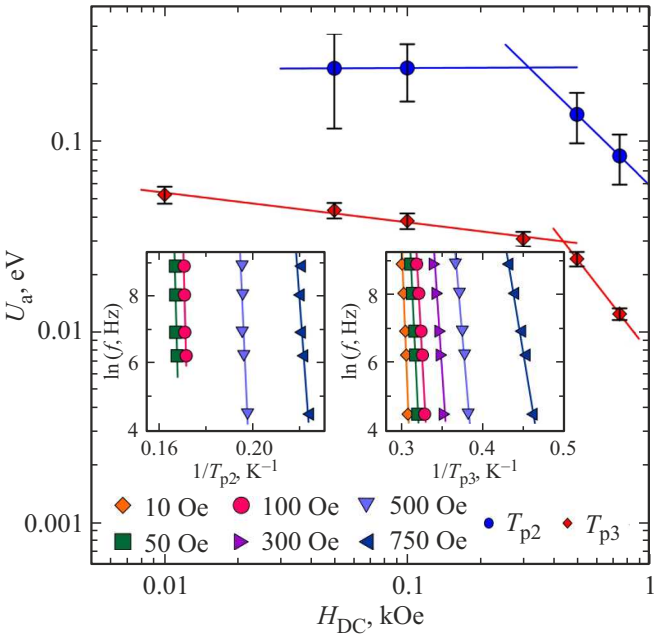

Figure 9. Field dependence of the activation energy U_a for the second (circles) and third (diamonds) transitions. The insets show Arrhenius curves for various bias fields, plotted for T_{p2} (left) and T_{p3} (right). Alternating field amplitude $H_{AC} = 1$ Oe.

($\alpha = 0.01$ for the second transition and $\alpha = 0.16$ for the third transition) for magnetic fields up to 300 Oe. For magnetic fields over 500 Oe, the dependence intensifies and is described by exponents of 1.6 and 1.2 for the second and third transitions, respectively. A remarkable decrease in activation barries with increasing magnetic field was found previously for both bulk and nanostructured superconductors [30,31], including alloys with gallium [11,24,32,33]. The field at which the type of field dependence of the activation energy changes corresponds to the field at which the type of curvature of the critical lines in the phase diagram changes. This was previously observed in [12,24,32,33] and was associated with changes in the system of superconducting vortices related to the morphology of the nanocomposite.

5. Conclusion

Magnetic studies of the superconductivity of a eutectic alloy of gallium and Sn embedded into the pores of an opal matrix revealed three transitions to the superconducting state at temperatures $T'_{c1} = 7.7$, $T'_{c2} = 6.2$ and $T'_{c3} = 4.3$ K in zero field. The results differ from those obtained for bulk alloy Ga-Sn and Ga-Sn in an opal matrix with smaller diameter balls. It was suggested that the first transition is associated with a small number of gallium segregates with the structure which was found in pure gallium nanoparticles. The second transition is caused by segregates with the λ-Ga structure. The third transition was attributed to the transition to the superconducting state of Sn-enriched segregates. In this case, there is an increase of T'_{c3} compared to bulk Sn due to size effects. A positive curvature of the field dependence curves of the first and third critical temperatures in the region of low fields is observed in the phase diagram in the $H-T$ plane which turns into a negative curvature with an increase of the magnetic field. Positive curvature was described in a model taking into account the influence of the proximity effect. The temperature hysteresis was found between the FCC and FCW curves, consistent with the critical state model. The dependence of the dynamic susceptibility on the frequency and amplitude of the alternating field showed the thermal activation nature of the movement of the vortices. Arrhenius curves were plotted and activation energies were calculated for various displacement fields. The field dependence of the activation energy revealed a sharp decrease of the thermal activation barriers in the field, at which a change in the type of curvature of the critical lines $T'_{c1}(H)$ and $T'_{c3}(H)$ in the $H-T$ diagram occurs.

Funding

The study was supported financially support by Russian Science Foundation grant No. 21-72-20038. The measurements were carried out on the equipment of the Resource Centers „Center for Diagnostics of Functional Materials for Medicine, Pharmacology and Nanoelectronics“, „X-ray Diffraction Research Methods“ and „Nanotechnologies“ of Science Park of St. Petersburg State University.

Conflict of interest

The authors declare that they have no conflict of interest.

References

[1] S. Liu, K. Sweatman, S. McDonald, K. Nogita. Mater. **11**, *8*, 1384 (2018).
[2] G. Bo, L. Ren, X. Xu, Y. Du, S. Dou. Adv. Phys. X **3**, *1*, 1446359 (2018).
[3] L. Ren, J. Zhuang, G. Casillas, H. Feng, Y. Liu, X. Xu, Y. Liu, J. Chen, I. Du, L. Jiang, S.X. Dou. Adv. Funct. Mater. **26**, *44*, 8111 (2016).
[4] S.-I. Shamoto, M.K. Lee, Y. Fujimura, K. Kondo, T.U. Ito, K. Ikeuchi, S. Yasuda, L.-J. Chang. Mater. Res. Express **8**, *7*, 076303 (2021).
[5] T.J. Anderson, I. Ansara. J. Phase Equilib. **13**, *2*, 181 (1992).
[6] M.V. Likholetova, E.V. Charnaya, E.V. Shevchenko, M.K. Lee, L.-J. Chang, Yu.A. Kumzerov, A.V. Fokin. Nanomater. **13**, *2*, 280 (2023).
[7] E.V. Charnaya, C. Tien, K.J. Lin, C.S. Wur, Y.A. Kumzerov. Phys. Rev. B **58**, *1*, 467 (1998).
[8] R. Würdenweber, V. Moshchalkov, S. Bending, F. Tafuri. Superconductors at the Nanoscale. From Basic Research to Applications. De Gruyter, Berlin (2017). 494 p.
[9] B. Zhang, J. Lyu, A. Rajan, X. Li, X. Zhang, T. Zhang, Z. Dong, J. Pan, Y. Liu, J. Zhang, R. Lortz, Z. Lai, P. Sheng. Mater. Today Phys. **6**, 38 (2018).
[10] S. Bose. Supercond. Sci. Technol **36**, *6*, 063003 (2023).

[11] O.D. Shevtsova, M.V. Likholetova, E.V. Charnaya, E.V. Shevchenko, Yu.A. Kumzerov, A.V. Fokin. Phys. Solid State **64**, *1*, 38 (2022).
[12] D.V. Smetanin, M.V. Likholetova, E.V. Charnaya, M.K. Lee, L.J. Chang, E.V. Shevchenko, Yu.A. Kumzerov, A.V. Fokin. Phys. Solid State **64**, *8*, 942 (2022).
[13] G. Knapp, M.F. Merriam. Phys. Rev. A **140**, *2A*, 528 (1965).
[14] E.V. Charnaya, C. Tien, M.K. Lee, Y.A. Kumzerov. J. Phys. Condens. Matter **21**, *45*, 455304 (2009).
[15] L. Bosio. J. Chem. Phys. **68**, *3*, 1221 (1978).
[16] R.D. Heyding, W. Keeney, S.L. Segel. Phys. Chem. Solids J. **34**, *1*, 133 (1973).
[17] H. He, G.T. Fei, P. Cui, K. Zheng, L.M. Liang, Y. Li, L.D. Zhang. Phys. Rev. B **72**, *7*, 073310 (2005).
[18] E.V. Charnaya, Y.A. Kumzerov, C. Tien, C.S. Wur. Solid State Commun. **94**, *8*, 635 (1995).
[19] K. Ohshima, T. Fujita. J. Phys. Soc. Jpn. **55**, *8*, 2798 (1986).
[20] R.W. Cohen, B. Abeles, G.S. Weisbarth. Phys. Rev. Lett. **18**, *10*, 336 (1967).
[21] D. Teske, J.E. Drumheller. J. Phys. Condens. Matter **11**, *25*, 4935 (1999).
[22] J.R. Clem, Z. Hao. Phys. Rev. B **48**, *18*, 13774 (1993).
[23] S. Sundar, M.K. Chattopadhyay, L.S.S. Chandra, S.B. Roy. Supercond. Sci. Technol. **28**, *7*, 075011 (2015).
[24] E.V. Shevchenko, E.V. Charnaya, M.K. Lee, L.-J. Chang, M.V. Likholetova, I.E. Lezova, Y.A. Kumzerov, A.V. Fokin. Physica C **574**, 1353666 (2020).
[25] M.R. Koblischka, L. Púst, C.-S. Chang, T. Hauet, A. Koblischka-Veneva. Metals **13**, *6*, 1140 (2023).
[26] S. Chu, A.J. Schwartz, T.B. Massalski, D.E. Laughlin. Appl. Phys. Lett. **89**, *11*, 111903 (2006).
[27] S. Theodorakis, Z. Tešanović. Phys. Rev. B **40**, *10*, 6659 (1989).
[28] E.H. Brandt. Phys. Rev. B **55**, *21*, 14513 (1997).
[29] J.R. Clem, B. Bumble, S.I. Raider, W.J. Gallagher, Y.C. Shih. Phys. Rev. B **35**, *13*, 6637 (1987).
[30] G. Prando, P. Carretta, R. De Renzi, S. Sanna, H.-J. Grafe, S. Wurmehl, B. Büchner. Phys. Rev. B **85**, *14*, 144522 (2012).
[31] S.R. Ghorbani, X.L. Wang, M. Shabazi, S.X. Dou, K.Y. Choi, C.T. Lin. Appl. Phys. Lett. **100**, *7*, 072603 (2012).
[32] M.K. Lee, E.V. Charnaya, C. Tien, L.J. Chang, Y.A. Kumzerov. J. Appl. Phys. **113**, *11*, 113903 (2013).
[33] M.K. Lee, E.V. Charnaya, S. Muhlbauer, U. Jeng, L.J. Chang, Y.A. Kumzerov. Sci. Rep. **11**, *1*, 4807 (2021).

Translated by A.Akhtyamov